Topological Photonics: A Mathematical Perspective

Ross Parker and Alejandro Aceves

1. Introduction

Topological photonics is a framework that follows both condensed matter physics and topology. It refers to designing the guiding properties of the propagating medium (e.g., a photonic crystal or a waveguide lattice) in such a way that the transport of electromagnetic energy is realized in unique, robust, and sometimes unexpected ways. Consider a simple thought experiment: imagine first the two-dimensional wave equation on a square domain, and assume homogeneous Dirichlet boundary conditions. We know that the accessible modes extend in periodic form throughout the whole domain and, in time, waves can propagate in all directions. This behavior is in response to the inherent symmetries of the medium. Imagine instead that we engineer the medium in such a way that all the energy concentrates in the boundary of the medium and propagates in only one direction. (In the language of optics, this would be seen as inhibiting back reflection and making the bulk medium act like an insulator).

Typically, in describing a photonic system, we refer to physical quantities such as frequency, wave vector, polarization, and dispersion. Instead, in the relatively new field of topological photonics, the term "topology" refers to a property of a photonic material that characterizes global behavior of the wavefunctions on their entire dispersion map; most importantly, this property takes quantized values. Think of this as characterizing the "genus" of an object, like a doughnut, with the "object" being described in wave vector space rather than in physical space. There are analogues in photonics to the topological fact that continuous deformations will not change the genus of an object. As an example, photonic topological insulators that are designed using artificial materials can support topologically nontrivial unidirectional states of light. These states are characterized by a particular "genus-like" number. Since this number is quantized, this unidirectional property will be robust to perturbations in the underlying photonic structure.

Photonics research often parallels or aims at explaining phenomena in other physical contexts. Bose-Einstein condensation in condensed matter physics is governed by the Gross-Pitaevskii equation, which is identical to the nonlinear Schrödinger equation that governs intense laser beam propagation in a dielectric medium such as air. In the quantum realm, nontrivial states of two-dimensional matter (e.g., a periodic lattice of atoms) with broken time-reversal symmetry can have the property that the bulk is an insulator while states (modes) exist that carry current along the sample edges without dissipation. The characteristic "genus-like" integer is called the Chern number (see section 3 for an example), which arises out of topological properties of the material's band structure (see the discussion in section 2 and section 3 below).

In photonic crystals, a periodic variation of the dielectric properties of the medium affects photons in the same manner as solids modulate electrons (with the caveat that photons are bosons, while electrons are fermions). The question is whether the topological features are replicated in the analogous photonic system. In two foundational papers by Haldane and Raghu [HR08, RH08], the authors highlight the photonics analogue to quantum properties. They demonstrate the ingredients necessary to create a "one-way waveguide" which exhibits properties similar to the Quantum Hall Effect. While the model in [HR08] has not been experimentally realized, it motivated further work by Wang, Chong, Joannopoulos, and Soljačić, in which they first predicted the existence of edge states in a magneto-optical crystal in the microwave regime [WCJS08] and then demonstrated these experimentally [WCJS09]. Experiments by Rechtsman et al. [RZP+13] found topological edge states without the need for an external magnetic field by using a photonic crystal comprising helical waveguides.

Since then, the field of topological photonics has matured and continues to be very active, both in theory and experiments, as well as in the linear and nonlinear regimes. While we have briefly discussed its origins, it is not our

Ross Parker is a research staff member at the IDA Center for Communications Research, Princeton. His email address is r.parker@ccr-princeton.org.
Alejandro Aceves is a professor in the department of mathematics at Southern Methodist University. His email address is aaceves@smu.edu.

Communicated by Notices *Associate Editor Reza Malek-Madani.*

DOI: https://doi.org/10.1090/noti2998

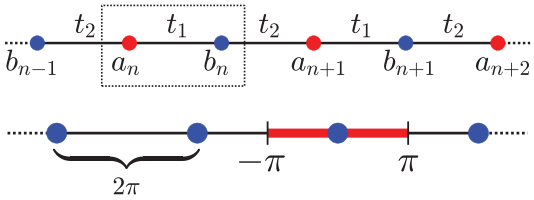

Figure 1. Top: schematic of SSH model, unit cell (a_n, b_n) in dotted box. Coupling constant is t_1 within unit cell, and t_2 between unit cells. Bottom: reciprocal lattice, first BZ $[-\pi, \pi]$ shown in red.

purpose to give a detailed history of the field (for this purpose, we point the interested reader to the review articles [JS14, LCG+22]). Instead, we will focus our discussion on three prototypical examples: the one-dimensional Su-Schrieffer-Heeger model, the two-dimensional Haldane model, and the model of a photonic Floquet topological insulator from [RZP+13]. We hope that this article highlights why this is a fertile area for mathematicians to explore and contribute to with their expertise.

2. SSH Model

The Su-Schrieffer-Heeger (SSH) model [SSH79], is the simplest lattice model that exhibits topological features. It was devised to describe the electrical conductivity in a doped polyacetylene polymer chain. The lattice comprises repeating, two-node unit cells, where the couplings within and between unit cells are given by t_1 and t_2, respectively (Figure 1, top). The optical analogue is a linear lattice of waveguides in which the nearest-neighbor couplings are staggered (this can be implemented, e.g., by altering the physical spacings between the fibers). Mathematically, the SSH model can be described by the discrete nonlinear Schrödinger equation

$$\begin{aligned} i\dot{a}_n + t_1 b_n + t_2 b_{n-1} + \gamma |a_n|^2 a_n &= 0 \\ i\dot{b}_n + t_1 a_n + t_2 a_{n+1} + \gamma |b_n|^2 b_n &= 0, \end{aligned} \tag{1}$$

where (a_n, b_n) is the nth unit cell, and $\gamma > 0$ is the strength of the cubic nonlinearity. (A rigorous mathematical derivation can be found in [AC22]).

Our analysis follows that of [AOP16, Chapter 1] and [AC22, Section 8]. The topological features of the optical SSH model can be understood by studying the linear model ($\gamma = 0$). As a first step, we look for plane wave solutions of the form

$$\mathbf{w}(k) = \begin{pmatrix} a_n \\ b_n \end{pmatrix} = \begin{pmatrix} a \\ b \end{pmatrix} e^{i(kn - \lambda t)}, \tag{2}$$

where λ is the frequency and k is the wavenumber. Equation (2) is periodic in k with period 2π, since $\mathbf{w}(k+2m\pi) = \mathbf{w}(k)$ for any integer m. The points $\{2m\pi : m \in \mathbb{Z}\}$ define another linear lattice, which is called the reciprocal lattice (Figure 1, bottom). The first Brillouin zone (BZ) is the set of points closer to the origin than any other point of the

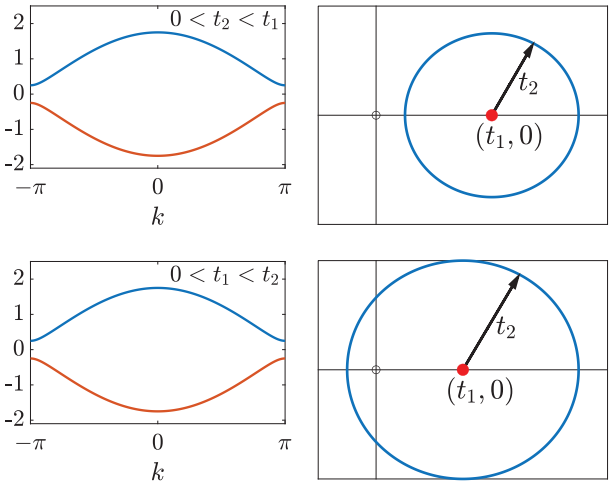

Figure 2. Left: band structure of the SSH model for $0 < t_2 < t_1$ (top) and $0 < t_1 < t_2$ (bottom). Right: circle in the complex plane traced counterclockwise by $h(k)$ for $k \in [-\pi, \pi]$.

reciprocal lattice, which in this case is the interval $[-\pi, \pi]$. Due to the 2π-periodicity, the BZ is topologically equivalent to the unit circle S^1.

Substituting the ansatz (2) into (1) and simplifying, we obtain the k-dependent eigenvalue problem $H(k)\mathbf{v} = -\lambda(k)\mathbf{v}$, where $\mathbf{v} = (a, b)^\top$, and $H(k)$ is the Hermitian matrix

$$H(k) = \begin{pmatrix} 0 & h(k) \\ h^*(k) & 0 \end{pmatrix}, \qquad h(k) = t_1 + t_2 e^{-ik}.$$

Since $H(k)$ is 2π-periodic, we only need to consider $k \in [-\pi, \pi]$, i.e., in the first BZ. We note that since we are posing the problem on the full integer lattice, k can take any value in $[-\pi, \pi]$. The eigenvalues of $H(k)$ are

$$\lambda(k) = \pm |h(k)| = \sqrt{t_1^2 + t_2^2 + 2t_1 t_2 \cos k}, \tag{3}$$

which is the dispersion relation $\lambda(k)^2 = |h(k)|^2$ relating the frequency λ and the wavenumber k. Each eigenvalue $\lambda(k)$ is a continuous function of the wavenumber on the first BZ, and is called a band. Since $H(k)$ is a 2×2 matrix, the SSH model has two bands. All of the bands of the system form its band structure, which is illustrated in the left column of Figure 2. (These terms are borrowed from solid state physics, where the band structure describes the energy levels that electrons can occupy in a solid).

When $t_1 \neq t_2$, there is a space between the upper and lower bands, which is known as a band gap. This band gap has size 2Δ, where $\Delta = |t_1 - t_2|$. The band gap closes when $t_1 = t_2$. Since the eigenvalues (3) are unchanged if t_1 and t_2 are exchanged, it appears at first glance that the cases $t_1 > t_2$ and $t_1 < t_2$ are identical, i.e., that the problem is symmetric about $t_1 = t_2$. Interestingly, this is not the case. For a complete picture, we need to look at the eigenvectors of $H(k)$ as well.

The normalized eigenvectors corresponding to the eigenvalues $\pm\lambda(k)$ are given by

$$\mathbf{v}_\pm(k) = \frac{1}{\sqrt{2}}\begin{pmatrix}\pm\hat{h}(k)\\ 1\end{pmatrix}, \quad \hat{h}(k) = \frac{h(k)}{|h(k)|}. \tag{4}$$

Since $\hat{h}(k)$ is a complex number of unit modulus whose argument is the same as that of $h(k)$, we can write $\mathbf{v}_\pm(k)$ as

$$\begin{aligned}\mathbf{v}_\pm(k) &= \frac{1}{\sqrt{2}}\begin{pmatrix}\pm e^{i\phi(k)}\\ 1\end{pmatrix}\\ \tan\phi &= \frac{\operatorname{Im} h(k)}{\operatorname{Re} h(k)} = -\frac{t_2\sin k}{t_1 + t_2\cos k}.\end{aligned} \tag{5}$$

As the wavenumber k varies from $-\pi$ to π over the BZ, the complex number $h(k)$ traces a clockwise circle in the complex plane with center $(t_1, 0)$ and radius t_2. This circle encloses the origin when $t_1 < t_2$, but does not when $t_1 > t_2$ (Figure 2, right column). The topological invariant is the winding number of $h(k)$, which is the number of times $h(k)$ travels counterclockwise around the origin. We can see from Figure 2 that

$$\operatorname{Ind}_h(0) = \begin{cases}-1 & t_1 < t_2\\ 0 & t_1 > t_2\end{cases}, \tag{6}$$

where a winding number of -1 represents a single clockwise trip around the origin. (The winding number is undefined if $t_1 = t_2$).

The same topological information can be obtained in a different way by computing a quantity known as the Berry phase [Ber84] (also known as the Zak phase [Zak89] in 1D). Intuitively, the Berry phase is the phase angle accumulated by a complex vector, e.g., one of the eigenvectors $\mathbf{v}_\pm(k)$, around a closed contour in k-space. We will take a brief digression to discuss these concepts, following [AOP16, Chapter 2] and [Van18, Chapter 3], before computing them for the SSH model.

Let $\mathbf{v}(k)$ be a normalized eigenvector of $H(k)$. For any wavenumbers k_1 and k_2, we define the relative phase between $\mathbf{v}(k_1)$ and $\mathbf{v}(k_2)$ by

$$\gamma_{12} = \arg\langle \mathbf{v}(k_2), \mathbf{v}(k_1)\rangle, \tag{7}$$

where $\arg z$ is the phase, or argument, of the complex number z. (We are using the Hermitian inner product $\langle \mathbf{u}, \mathbf{v}\rangle = \mathbf{u}^\dagger\mathbf{v} = \sum_j u_j^* v_j$, where the dagger symbol denotes the conjugate transpose; the complex conjugation is placed on the first component to be consistent with the Dirac notation of quantum mechanics). The relative phase γ_{12} satisfies the equation

$$e^{i\gamma_{12}} = \frac{\langle \mathbf{v}(k_2), \mathbf{v}(k_1)\rangle}{|\langle \mathbf{v}(k_2), \mathbf{v}(k_1)\rangle|}. \tag{8}$$

It is important to note that the eigenvector $\mathbf{v}(k)$ is not unique. In particular, since it is a unit vector, it is specified only up to multiplication by a constant unit complex number $e^{i\theta}$. The transformation $\mathbf{v}(k) \mapsto e^{i\theta}\mathbf{v}(k)$ is called a gauge transformation. The relative phase γ_{12} is not invariant under a gauge transformation, since if we take $\mathbf{v}(k_j) \mapsto e^{i\theta_j}\mathbf{v}(k_j)$, $\langle \mathbf{v}(k_2), \mathbf{v}(k_1)\rangle$ transforms to

$$\langle e^{i\theta_2}\mathbf{v}(k_2), e^{i\theta_1}\mathbf{v}(k_1)\rangle = e^{i(\theta_1-\theta_2)}\langle \mathbf{v}(k_2), \mathbf{v}(k_1)\rangle,$$

thus $\gamma_{12} \mapsto \gamma_{12} + (\theta_1 - \theta_2)$.

We wish to define the change of phase of $\mathbf{v}(k)$ in such a way as to be gauge invariant. To do this, we take a sequence $(k_1, k_2, \ldots, k_N)$ of N points in k-space ordered in a loop. We then define the discrete Berry phase by

$$\begin{aligned}\gamma &= \arg e^{i(\gamma_{12}+\gamma_{23}+\cdots+\gamma_{N,1})}\\ &= \arg\left(\langle \mathbf{v}(k_2), \mathbf{v}(k_1)\rangle\langle \mathbf{v}(k_3), \mathbf{v}(k_2)\rangle\cdots\langle \mathbf{v}(k_1), \mathbf{v}(k_N)\rangle\right),\end{aligned}$$

which is the phase accumulated by $\mathbf{v}(k)$ around the loop. Unlike the relative phases γ_{jk}, the Berry phase is gauge invariant; if we take the gauge transformations $\mathbf{v}(k_j) \mapsto e^{\theta_j}\mathbf{v}(k_j)$, the Berry phase transforms to $\gamma + (\theta_1 - \theta_2) + (\theta_2 - \theta_3) + \cdots + (\theta_N - \theta_1)$, which is equal to γ, since all of the θ_j cancel. We note that the Berry phase is only unique up to an integer multiple of 2π unless we take the principal value of the argument, i.e., restrict $\arg z$ to $(-\pi, \pi]$.

We now move from discrete to continuous. In particular, we wish to compute the phase accumulated by $\mathbf{v}(k)$ along a continuous, closed path. For small Δk, let $\Delta\gamma$ be the relative phase accumulated between $\mathbf{v}(k)$ and $\mathbf{v}(k+\Delta k)$. Following (8), $\Delta\gamma$ satisfies the equation

$$e^{i\Delta\gamma} = \frac{\langle \mathbf{v}(k+\Delta k), \mathbf{v}(k)\rangle}{|\langle \mathbf{v}(k+\Delta k), \mathbf{v}(k)\rangle|}. \tag{9}$$

Since Δk is small and $\mathbf{v}$ is a unit vector, the denominator in (9) is approximately 1, thus

$$e^{i\Delta\gamma} \approx \langle \mathbf{v}(k+\Delta k), \mathbf{v}(k)\rangle.$$

Expanding both sides in a Taylor series to first order in $\Delta\gamma$ and Δk and simplifying, we find that $\Delta\gamma$ is approximately given by

$$\Delta\gamma \approx i\left\langle \mathbf{v}(k), \frac{d}{dk}\mathbf{v}(k)\right\rangle \Delta k. \tag{10}$$

We define the Berry connection by

$$A(k) = i\left\langle \mathbf{v}(k), \frac{d}{dk}\mathbf{v}(k)\right\rangle = i\mathbf{v}(k)^\dagger\frac{d}{dk}\mathbf{v}(k), \tag{11}$$

which is the coefficient of Δk on the RHS of (10). We then define the Berry phase to be the integral of Berry connection around a closed contour $\mathcal{C}$:

$$\gamma = \oint_{\mathcal{C}} A(k)dk. \tag{12}$$

As in the discrete case, the Berry connection is not gauge invariant, while the Berry phase is invariant under gauge transformations (modulo integer multiples of 2π).

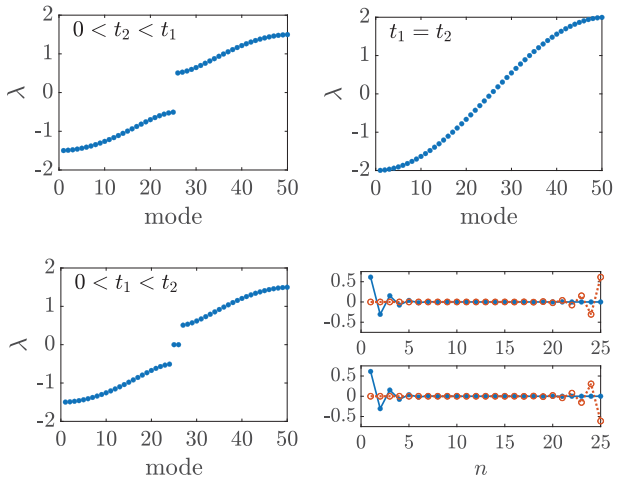

Figure 3. Eigenvalues of B for $0 < t_2 < t_1$ (top left), $t_1 = t_2$ (top right), and $0 < t_1 < t_2$ (bottom left). Edge mode eigenvectors $\mathbf{v} = (\mathbf{a}, \mathbf{b})$ for $0 < t_1 < t_2$ (bottom right); $\mathbf{a}$ (solid blue line) and $\mathbf{b}$ (dotted orange line) are either in-phase (top) or out-of-phase (bottom). $N = 25$ unit cells with Dirichlet boundary conditions.

Returning to the SSH model, we first compute the Berry connection using the eigenvector $\mathbf{v}_+(k)$:

$$A(k) = i\left\langle \frac{1}{\sqrt{2}}\begin{pmatrix} e^{i\phi(k)} \\ 1 \end{pmatrix}, \frac{1}{\sqrt{2}}\begin{pmatrix} i\phi'(k)e^{i\phi(k)} \\ 0 \end{pmatrix} \right\rangle$$
$$= -\frac{1}{2}\phi'(k).$$

We then compute the Berry phase by integrating the Berry connection from $-\pi$ to π. This is a closed contour in the BZ since the endpoints of $[-\pi, \pi]$ correspond to the same point on the unit circle S^1. The Berry phase is

$$\gamma = -\frac{1}{2}\int_{-\pi}^{\pi} \phi'(k)dk = \begin{cases} \pi & t_1 < t_2 \\ 0 & t_1 > t_2, \end{cases}$$

which is the change in phase of the eigenvector $\mathbf{v}_+(k)$ over the BZ. Since it is a constant multiple of (6), it conveys the same information as the winding number.

The fundamental topological difference between the two asymmetric lattice configurations ($t_1 < t_2$ and $t_1 > t_2$) becomes evident when we consider a finite lattice. Specifically, we take a lattice comprising $2N$ waveguides (N unit cells) with Dirichlet boundary conditions at the two ends ($b_0 = 0$ and $a_{N+1} = 0$). For the linear system, solutions are standing waves of the form $(\mathbf{a}, \mathbf{b})^\top e^{-i\lambda t}$, where $\mathbf{a} = (a_1, \dots, a_N)$ and $\mathbf{b} = (b_1, \dots, b_N)$ represent the a and b sublattices of the system. Substituting this ansatz into (1) yields the eigenvalue problem $B\mathbf{v} = -\lambda\mathbf{v}$, where $\mathbf{v} = (\mathbf{a}, \mathbf{b})^\top \in \mathbb{C}^{2N}$ and B is the off-diagonal block matrix

$$B = \begin{pmatrix} 0 & B_0 \\ B_0^\top & 0 \end{pmatrix}, \quad B_0 = \begin{pmatrix} t_1 & & \\ t_2 & t_1 & \\ & \ddots & \ddots \end{pmatrix}.$$

An intuitive understanding of the difference between the two cases can be gained by considering the two extreme configurations, where one of the coupling constants is set to 0. If $t_1 > 0$ and $t_2 = 0$, the lattice comprises N independent dimers with internal coupling constant t_1. The eigenvalues of B are $\pm t_1$, each with multiplicity N. On the other hand, if $t_1 = 0$ and $t_2 > 0$, the lattice instead comprises $N-1$ independent dimers (staggered from the ones in the previous case) with internal coupling constant t_2, as well as two unconnected nodes at the ends of the lattice. In addition to eigenvalues at $\pm t_2$, each with multiplicity $N-1$, the matrix B has two eigenvalues at 0. The eigenvectors corresponding to these zero eigenvalues are $(1, 0, \dots, 0)^\top$ and $(0, \dots, 0, 1)^\top$. These are called edge modes, since they are localized at the ends of the lattice.

Since B is a $2N \times 2N$ matrix, its spectrum is a discrete set of $2N$ eigenvalues, as opposed to the two continuous bands of eigenvalues found from the dispersion relation in the infinite lattice case. The eigenvalues of B are shown in Figure 3 for $0 < t_2 < t_1$, $t_1 = t_2$, and $0 < t_1 < t_2$. The two asymmetric configurations contain a "gap," which closes when $t_1 = t_2$. This eigenvalue gap is analogous to the band gap in the infinite lattice case. When $0 < t_2 < t_1$, there are no eigenvalues in this gap, and all of the eigenvectors are nonlocalized. When $0 < t_1 < t_2$, however, there are two eigenvalues close to (but not exactly at) 0 which lie within this gap (these eigenvalues approach 0 in the limit $N \to \infty$). As in the case where $t_1 = 0$, these eigenvalues correspond to edge modes, since $\mathbf{a}$ and $\mathbf{b}$ are localized to the left and right edges of the lattice, respectively (Figure 3, bottom right). All of the remaining modes are nonlocalized.

Finally, we briefly comment on what occurs when a cubic nonlinearity ($\gamma > 0$) is present (see [MS21] for a more thorough treatment). Standing wave solutions of the form $(\mathbf{a}, \mathbf{b})^\top e^{-i\lambda t}$ solve the equation $B\mathbf{v} + \gamma\mathbf{v}^3 + \lambda\mathbf{v} = 0$, where $\mathbf{v} = (a_1, \dots, a_N, b_1, \dots, b_N)$. Numerical continuation experiments show that the edge modes from the linear model persist for small γ.

3. Haldane Model

We now turn to a two-dimensional model. We start with a honeycomb lattice (Figure 4), which is constructed from a two-site unit cell, with sites labeled a and b. These unit cells tile the plane periodically along the two primitive lattice vectors $\mathbf{v}_1 = \left(\frac{3}{2}, \frac{\sqrt{3}}{2}\right)$ and $\mathbf{v}_2 = \left(\frac{3}{2}, -\frac{\sqrt{3}}{2}\right)$ to obtain a hexagonal lattice. We note that the a-sites and b-sites form two offset, triangular sublattices. This structure is similar to that of the material graphene, which is a hexagonal lattice constructed entirely from carbon atoms. The spatial location of a unit cell is specified by the vector $\mathbf{r}_\mathbf{n} = m\mathbf{v}_1 + n\mathbf{v}_2$, where $\mathbf{n} = (m, n) \in \mathbb{Z}^2$. It is therefore natural to index the unit cells by the vector $\mathbf{n}$; the locations of the lattice sites $a_\mathbf{n}$ and $b_\mathbf{n}$ in unit cell $\mathbf{n}$ are $r_\mathbf{n}$ and $r_\mathbf{n} + (1, 0)$,

respectively. Each node in the honeycomb lattice is connected to its three nearest neighbors with coupling strength $t_1 > 0$, which is a coupling between sublattices. The directions of the nearest-neighbor (NN) couplings are given by the vectors $\delta_1 = \left(\frac{1}{2}, -\frac{\sqrt{3}}{2}\right)$, $\delta_2 = \left(\frac{1}{2}, \frac{\sqrt{3}}{2}\right)$, and $\delta_3 = -(\delta_1 + \delta_2) = (-1, 0)$, which are depicted in Figure 4. The resulting linear model can be written as

$$i\dot{a}_{\mathrm{n}} + t_1 \sum_{\langle \mathrm{m} \rangle} b_{\mathrm{m}} = 0, \qquad i\dot{b}_{\mathrm{n}} + t_1 \sum_{\langle \mathrm{m} \rangle} a_{\mathrm{m}} = 0, \tag{13}$$

where the angle brackets indicate that the sum is taken over nearest neighbors. The system (13) obeys time-reversal symmetry, i.e., is invariant under the transformation $t \mapsto -t$, $(a_{\mathrm{n}}, b_{\mathrm{n}}) \mapsto (a_{\mathrm{n}}^*, b_{\mathrm{n}}^*)$.

The Haldane model [Hal88] adds two more terms to the honeycomb model. We will see that this results in a band gap in the spectrum, similar to what occurs in the SSH model with unequal couplings. First, the Haldane model has an on-site energy term of magnitude t_0, which takes opposite signs on the a and b sublattices. In addition, there is an imaginary, next-nearest neighbor (NNN) coupling term with strength it_2. (In the original Haldane model, this coupling term has the complex strength $t_2 e^{i\phi}$; we take $\phi = \pi/2$ here for simplicity). Each node is coupled to its six next-nearest neighbors, which is a coupling within sublattices. These couplings are staggered so that there is no net flux into or out of a single lattice site. The directions of the next-nearest neighbor couplings are given by the vectors $\delta_1' = \mathbf{v}_1$, $\delta_2' = -\mathbf{v}_2$, and $\delta_3' = \mathbf{v}_2 - \mathbf{v}_1$ (Figure 4). Using this notation, the linear model for the Haldane lattice is

$$\begin{aligned} i\dot{a}_{\mathrm{n}} + t_0 a_{\mathrm{n}} + t_1 \sum_{\langle \mathrm{m} \rangle} b_{\mathrm{m}} \pm i t_2 \sum_{\langle\langle \mathrm{m} \rangle\rangle} a_{\mathrm{m}} = 0 \\ i\dot{b}_{\mathrm{n}} - t_0 b_{\mathrm{n}} + t_1 \sum_{\langle \mathrm{m} \rangle} a_{\mathrm{m}} \pm i t_2 \sum_{\langle\langle \mathrm{m} \rangle\rangle} b_{\mathrm{m}} = 0, \end{aligned} \tag{14}$$

where the double angle brackets indicate that the sum is taken over next-nearest neighbors. The signs of the NNN couplings are indicated by the arrows in Figure 4, where outward and inward pointing arrows denote couplings of $+it_2$ and $-it_2$, respectively. The arrangement of the arrows in two staggered, counterclockwise triangles ensures no net flux results from the NNN term. Time-reversal symmetry is broken when $t_2 \neq 0$, but is unaffected by the on-site term t_0.

As in the SSH model, the first step is to compute the band structure, which is found by looking for plane wave solutions to (14) of the form

$$\mathbf{w}(\mathbf{k}) = \begin{pmatrix} a_{\mathrm{n}} \\ b_{\mathrm{n}} \end{pmatrix} = \begin{pmatrix} a \\ b \end{pmatrix} e^{i(\mathbf{k}\cdot \mathbf{r}_{\mathrm{n}} - \lambda t)}, \tag{15}$$

where $\mathbf{k} = (k_x, k_y)$ is the wave vector. As in the one-dimensional case, we restrict ourselves to a bounded region in $\mathbf{k}$-space, since $\mathbf{w}(\mathbf{k})$ is periodic in $\mathbf{k}$. Specifically, $\mathbf{w}(\mathbf{k} + \mathbf{r}^*) = \mathbf{w}(\mathbf{k})$, where $\mathbf{r}^*$ is called a reciprocal lattice vector. To determine the reciprocal lattice vectors, we note that $\mathbf{w}(\mathbf{k} + \mathbf{r}^*) = \mathbf{w}(\mathbf{k})$ if and only if

$$e^{i\mathbf{k}\cdot \mathbf{r}_{\mathrm{n}}} = e^{i(\mathbf{k}+\mathbf{r}^*)\cdot \mathbf{r}_{\mathrm{n}}} = e^{i\mathbf{k}\cdot \mathbf{r}_{\mathrm{n}}} e^{i\mathbf{r}^*\cdot \mathbf{r}_{\mathrm{n}}}.$$

This implies that $e^{i\mathbf{r}^*\cdot \mathbf{r}_n} = 1$, i.e., $\mathbf{r}^* \cdot \mathbf{r}_n = m(\mathbf{r}^*\cdot \mathbf{v}_1) + n(\mathbf{r}^*\cdot \mathbf{v}_2)$ is an integer multiple of 2π. To satisfy this criterion, we take $\mathbf{r}^* = l_1 \mathbf{v}_1^* + l_2 \mathbf{v}_2^*$ for integers l_1 and l_2, where

$$\mathbf{v}_i^* \cdot \mathbf{v}_j = 2\pi \delta_{ij} = \begin{cases} 2\pi & i = j \\ 0 & i \neq j. \end{cases}$$

The points $\mathbf{r}^*$ define another lattice, which is called the reciprocal lattice, and its periodicity is given by the primitive reciprocal lattice vectors $\mathbf{v}_1^*$ and $\mathbf{v}_2^*$. For a two-dimensional lattice, $\mathbf{v}_1^*$ and $\mathbf{v}_2^*$ can be computed in terms of the primitive lattice vectors $\mathbf{v}_1$ and $\mathbf{v}_2$ using the formulas

$$\mathbf{v}_1^* = \frac{2\pi Q \mathbf{v}_2}{\mathbf{v}_1 \cdot Q\mathbf{v}_2}, \quad \mathbf{v}_2^* = \frac{2\pi Q \mathbf{v}_1}{\mathbf{v}_2 \cdot Q\mathbf{v}_1}, \quad Q = \begin{pmatrix} 0 & -1 \\ 1 & 0 \end{pmatrix}.$$

For the honeycomb lattice, $\mathbf{v}_1^* = \frac{2\pi}{3}(1, \sqrt{3})$ and $\mathbf{v}_2^* = \frac{2\pi}{3}(1, -\sqrt{3})$. The first BZ is the set of points closer to the origin than any other point of the reciprocal lattice (outlined hexagon in Figure 5, top left). This is the Voronoi cell around the origin, which is a unit cell of the reciprocal lattice. Equivalently, the first BZ is the rhombus spanned by the reciprocal lattice vectors $\mathbf{v}_1^*$ and $\mathbf{v}_1^*$. Since opposite sides of this rhombus are identified due to periodicity, the first BZ has the topology of a torus.

Substituting the ansatz (15) into (14) and simplifying, we obtain the $\mathbf{k}$-dependent eigenvalue problem $H(\mathbf{k})\mathbf{v} = -\lambda(\mathbf{k})\mathbf{v}$, where

$$H(\mathbf{k}) = \begin{pmatrix} t_0 - f(\mathbf{k}) & h(\mathbf{k}) \\ h^*(\mathbf{k}) & -t_0 + f(\mathbf{k}) \end{pmatrix}$$
$$h(\mathbf{k}) = t_1 \sum_j e^{-i\mathbf{k}\cdot \delta_j}, \quad f(\mathbf{k}) = 2t_2 \sum_j \sin\left(\mathbf{k} \cdot \delta_j'\right).$$

We note that $h(-\mathbf{k}) = h^*(\mathbf{k})$ and $f(-\mathbf{k}) = -f(\mathbf{k})$. Since $H(\mathbf{k})$ is periodic in $\mathbf{k}$ along the reciprocal lattice vectors, we

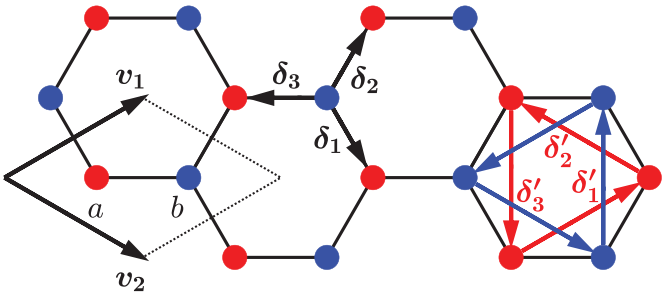

Figure 4. Schematic of the Haldane lattice. Rhombus is unit cell with sites a and b. Primitive lattice vectors $\mathbf{v}_1$ and $\mathbf{v}_2$. Nearest neighbor coupling vectors δ_1, δ_2, and δ_3. Next-nearest neighbor coupling vectors δ_1', δ_2', and δ_3'.

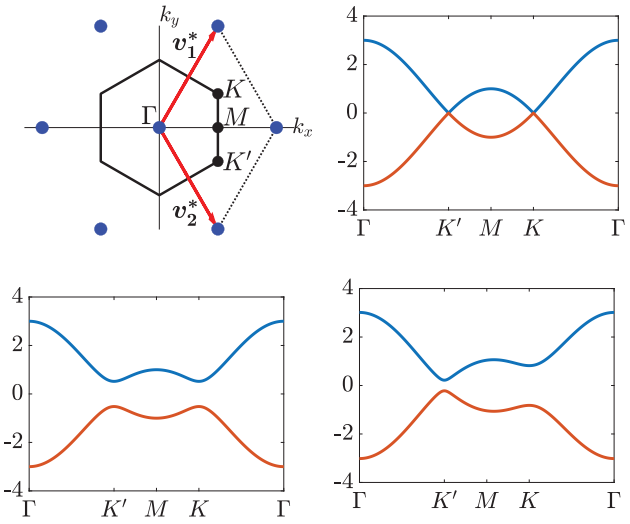

Figure 5. Top left: reciprocal lattice for Haldane model (blue dots). Red arrows are primitive reciprocal lattice vectors $\mathbf{v}_1^*$ and $\mathbf{v}_2^*$. Outlined hexagon is first BZ, which is equivalent to rhombus. Γ is the origin of the reciprocal lattice, K and K' are the two Dirac points, and M is the midpoint of the Dirac points. Band structure of Haldane model for $t_0 = 0$, $t_2 = 0$ (top right), $t_0 = 0$, $t_2 = 0.1$ (bottom left), and $t_0 = 0.3$, $t_2 = 0.1$ (bottom right), following piecewise linear path $\Gamma \to K' \to M \to K \to \Gamma$ in BZ. $t_1 = 1$.

only need to compute the eigenvalues of $H(\mathbf{k})$ over the first BZ. The eigenvalues of $H(\mathbf{k})$ give us the two bands $\pm\lambda(\mathbf{k})$, where

$$\lambda(\mathbf{k}) = \sqrt{|h(\mathbf{k})|^2 + (t_0 - f(\mathbf{k}))^2}. \tag{16}$$

The corresponding normalized eigenvectors are

$$\mathbf{v}_\pm(\mathbf{k}) = \frac{1}{\sqrt{2\lambda(\mathbf{k})(\lambda(\mathbf{k}) \pm g(\mathbf{k}))}} \begin{pmatrix} \pm\lambda(\mathbf{k}) + g(\mathbf{k}) \\ h^*(\mathbf{k}) \end{pmatrix}$$
$$g(\mathbf{k}) = t_0 - f(\mathbf{k}).$$

Plots of the band structure of the Haldane model for several parameter configurations are shown in Figure 5. (As is typically done, e.g., in [HR08, Figure 1], the bands are plotted following a piecewise linear path in the BZ). The eigenvalue $\lambda(\mathbf{k})$ has six minima, which are called Dirac points. These are located at the corners of the hexagonal BZ (Figure 5, top left). We label the two Dirac points with $k_x > 0$ by $K = \frac{2\pi}{3}\left(1, \frac{1}{\sqrt{3}}\right)$ and $K' = \frac{2\pi}{3}\left(1, -\frac{1}{\sqrt{3}}\right)$. The Dirac points K and K' are not equivalent in the BZ, since they are not related by translation through reciprocal lattice vectors. (The remaining Dirac points are equivalent to either K or K'). Near the Dirac points, the bands are called Dirac cones, since, to leading order, they are linear in $\mathbf{k}$. At the Dirac points,

$$\lambda(K) = \left|t_0 + 3\sqrt{3}t_2\right|, \qquad \lambda(K') = \left|t_0 - 3\sqrt{3}t_2\right|. \tag{17}$$

It follows from (17) that there is no band gap when $t_0 = 0$ and $t_2 = 0$ (Figure 5, top right). For $t_0 = 0$ and $t_2 > 0$, there is a band gap of size $6\sqrt{3}t_2$ (Figure 5, bottom left). The Dirac cones at both K and K' touch when $t_2 = 0$. For fixed $t_0 > 0$ and $t_2 > 0$, the behavior at the two Dirac points is no longer symmetric (Figure 5, bottom right). It follows from (17) that $\lambda(K) > 0$, thus the Dirac cones at K can never touch. The Dirac cones at K', however, touch when $t_2 = t_2^*$, where $t_2^* = t_0/3\sqrt{3}$. Therefore, there is a band gap for both $0 < t_2 < t_2^*$ and $t_2 > t_2^*$, and the band gap closes when $t_2 = t_2^*$. The closure of the band gap corresponds to a topological transition, which we will discuss below.

To understand what is occurring topologically, we will extend the concepts we discussed in section 2 from one to two dimensions (for a more rigorous treatment, see [AOP16] and [Van18]). Let $\mathbf{v}(\mathbf{k})$ be a normalized eigenvector of $H(\mathbf{k})$. As in the one-dimensional case, we are interested in how the phase of $\mathbf{v}(\mathbf{k})$ changes along a closed path in the BZ. For any $\mathbf{k}_1$ and $\mathbf{k}_2$, we define the relative phase between $\mathbf{v}(\mathbf{k}_1)$ and $\mathbf{v}(\mathbf{k}_2)$ by

$$\gamma_{12} = \arg\langle \mathbf{v}(\mathbf{k}_2), \mathbf{v}(\mathbf{k}_1)\rangle. \tag{18}$$

Analogous to equation (11), we define the Berry connection $\mathbf{A} = (A_x, A_y)$ by

$$\mathbf{A}(\mathbf{k}) = i\mathbf{v}(\mathbf{k})^\dagger D_\mathbf{k}\mathbf{v}(\mathbf{k}), \tag{19}$$

where $D_\mathbf{k}\mathbf{v}(\mathbf{k})$ is the Jacobian matrix for $\mathbf{v}(\mathbf{k})$. The Berry phase is the integral of the Berry connection around a closed contour $\mathcal{C}$ in $\mathbf{k}$-space:

$$\gamma = \oint_\mathcal{C} \mathbf{A}(\mathbf{k}) \cdot d\mathbf{k}. \tag{20}$$

Using Stokes's theorem (i.e., Green's theorem in two dimensions), we can write the Berry phase as

$$\gamma = \int_S \Omega(\mathbf{k}) dS, \tag{21}$$

where S is the region in the plane enclosed by $\mathcal{C}$, and

$$\Omega(\mathbf{k}) = \partial_x A_y - \partial_y A_x \tag{22}$$

is called the Berry potential. Evaluating the derivatives in (22) and using the equivalence of mixed partials, we can also write the Berry potential as

$$\Omega(\mathbf{k}) = -2\,\mathrm{Im}\left([\partial_{k_x}\mathbf{v}(\mathbf{k})]^\dagger \partial_{k_y}\mathbf{v}(\mathbf{k})\right). \tag{23}$$

The topological quantity of interest is the integral of the Berry connection around the boundary of the first BZ. By the Chern theorem (see, for example, [Nak90], as well as the intuitive explanation below), this is an integer multiple of 2π. We then define the Chern number of $\mathbf{v}(k)$ by

$$C = \frac{1}{2\pi}\oint_{\partial \mathrm{BZ}} \mathbf{A}(\mathbf{k}) \cdot d\mathbf{k} = \frac{1}{2\pi}\int_{\mathrm{BZ}} \Omega(\mathbf{k}) dS, \tag{24}$$

which is an integer.

We will use a numerical method to compute the Chern number [FHS05]. We first choose a mesh size N, and then

discretize the first BZ (rhombus in Figure 5, top left) using the $(N+1)^2$ points

$$\mathbf{k}_{m,n} = \frac{m}{N}\mathbf{v}_1^* + \frac{n}{N}\mathbf{v}_2^* \qquad m,n = 0,1,\ldots,N.$$

The discretized grid comprises N^2 rhombus-shaped plaquettes $P_{m,n}$, with corners $\mathbf{k}_{m,n}$, $\mathbf{k}_{m+1,n}$, $\mathbf{k}_{m+1,n+1}$, and $\mathbf{k}_{m,n+1}$. Let $\gamma_{m,n}^{m',n'}$ be the relative phase between $\mathbf{v}(\mathbf{k}_{m,n})$ and $\mathbf{v}(\mathbf{k}_{m',n'})$. Then the discrete Berry phase around the boundary of the BZ is defined by

$$\gamma_N = \arg\exp\left[i\left(\sum_{m=0}^{N-1}\gamma_{m,0}^{m+1,0} + \sum_{n=0}^{N-1}\gamma_{N,n}^{N,n+1} + \sum_{m=0}^{N-1}\gamma_{m+1,N}^{m,N} + \sum_{n=0}^{N-1}\gamma_{0,n+1}^{0,n}\right)\right], \tag{25}$$

where the subscript N denotes the mesh size. Instead of computing this, which involves the sum of $4N$ gauge-dependent relative phases, we will take the sum of the discrete Berry phases around each plaquette [AOP16, Chapter 2.1.3]. The discrete Berry phase around $P_{m,n}$ is given by

$$F_{mn} = \arg\exp\left[i\left(\gamma_{m,n}^{m+1,n} + \gamma_{m+1,n}^{m+1,n+1} + \gamma_{m+1,n+1}^{m,n+1} + \gamma_{m,n+1}^{m,n}\right)\right], \tag{26}$$

where we take the principal value of the argument, i.e., take $F_{mn} \in (-\pi, \pi]$. Taking the product of the Berry phases F_{mn} for all N^2 plaquettes,

$$\begin{aligned}\prod_{m,n=0}^{N-1} e^{iF_{mn}} &= \exp\left(i\sum_{m,n=0}^{N-1} F_{mn}\right) \\ &= \exp\Big(i\sum_{m,n=0}^{N-1}\left[\gamma_{m,n}^{m+1,n} + \gamma_{m+1,n}^{m+1,n+1} + \gamma_{m+1,n+1}^{m,n+1} + \gamma_{m,n+1}^{m,n}\right]\Big).\end{aligned} \tag{27}$$

Consider an internal edge of the mesh connecting the points $\mathbf{k}_{m,n}$ and $\mathbf{k}_{m',n'}$. This edge appears in exactly two adjacent plaquettes, but in opposite orientations, which implies that the sum on the RHS of (27) contains the relative phases $\gamma_{m,n}^{m',n'}$ and $\gamma_{m',n'}^{m,n}$, each exactly once. Since the Hermitian inner product is conjugate-symmetric, $\gamma_{m,n}^{m',n'} = -\gamma_{m',n'}^{m,n}$, thus the relative phase contributions from all internal edges cancel. This implies that the exponents on the RHS of equations (25) and (27) are the same, i.e.,

$$e^{i\gamma_N} = \exp\left(i\sum_{m,n=0}^{N-1} F_{mn}\right), \tag{28}$$

from which it follows that the discrete Berry phase γ_N and the plaquette sum $\sum_{m,n=0}^{N-1} F_{mn}$ are equal, modulo an integer multiple of 2π.

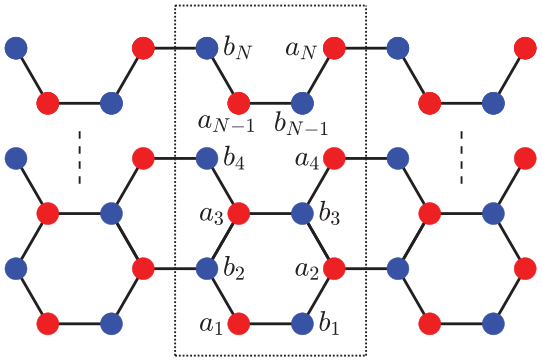

Figure 6. Ribbon of Haldane lattice with armchair edges on top and bottom, infinite in horizontal direction. Unit cell enclosed in dotted lines.

Finally, we use the discrete Berry phase around the BZ to define the discrete Chern number

$$C_N = \frac{1}{2\pi}\sum_{m,n=0}^{N-1} F_{mn}. \tag{29}$$

Since the BZ is a torus, opposite boundaries of the BZ are identified. In particular, this means that opposite external edges of the mesh are equivalent, e.g., the edge between $\mathbf{k}_{0,n}$ and $\mathbf{k}_{0,n+1}$ is the same as that between $\mathbf{k}_{N,n}$ and $\mathbf{k}_{N,n+1}$. Since the two members of each pair of equivalent external edges appear exactly once, but in opposite orientations, in the sum on the RHS of (27), the relative phase contributions from all external edges cancel as well. This implies that the exponent in (28) is 0, so that γ_N is an integer multiple of 2π, and C_N is an integer. We can think of the Chern number C as the limit of C_N as $N \to \infty$, which provides an intuitive explanation for why the Chern number is integer valued.

Returning to the Haldane model, we compute the Chern numbers of the two bands using the above discretization with $N = 100$. First, we consider the case when $t_0 = 0$. When $t_2 = 0$, the Chern numbers of both bands are 0, and when $t_2 > 0$, the Chern numbers of the upper and lower bands are 1 and -1, respectively. When $t_0 > 0$, the Chern number of the upper band is

$$C = \begin{cases} 0 & 0 < t_2 < t_2^* \\ 1 & t_2 > t_2^*, \end{cases}$$

and the Chern number of the lower band has the same magnitude but opposite sign. The Chern number changes from 0 to 1 when the band gap closes at $t_2 = t_2^*$. This transition from the nontopological to the topological regime is analogous to what occurs in the SSH model.

The fundamental difference between the nontopological and topological states can be most easily seen in a lattice which is finite in at least one dimension. As in the one-dimensional case, imposition of a boundary will give rise to edge modes. The simplest example is a ribbon lattice,

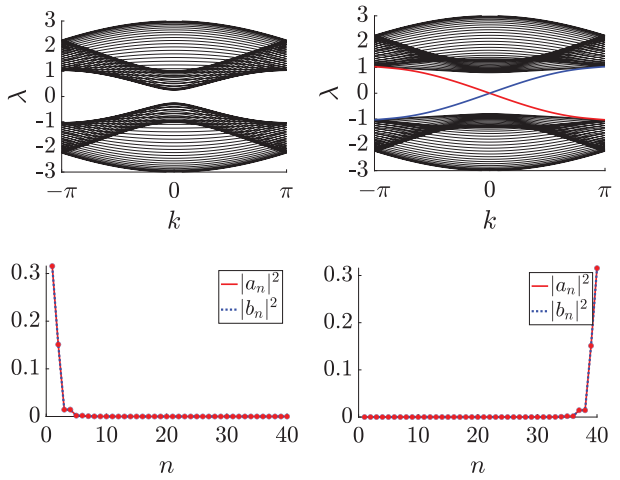

Figure 7. Band structure for ribbon of Haldane lattice with armchair edges. Top left: $t_0 = 0.25$ and $t_2 = 0$ (nontopological state). Top right: $t_0 = 0.25$ and $t_2 = 0.2$ (topological state). Blue and red lines are edge modes which connect the upper and lower bands. Band gap closes at $t_2 = t_2^* = 0.0481$. Bottom: eigenvector $(\mathbf{a}, \mathbf{b})^\top$ corresponding to the two edge modes from top right for $k = \pi/4$. $N = 40$ and $t_1 = 1$ in all cases.

which is finite in one direction and infinite in the other. There are many possible configurations for the edges of the ribbon (see, for example, [LFR24]), and we note that the edge mode behavior and properties depend on this choice. We will use armchair edges for the top and bottom edges of the ribbon, which are illustrated in Figure 6. The unit cell of the ribbon (dotted square in Figure 6) comprises N sites of each type, for a total of $2N$ sites.

Solutions to the linear system are standing waves of the form $(\mathbf{a}, \mathbf{b})^\top e^{i(kn-\lambda t)}$, where $\mathbf{a} = (a_1, \dots, a_N)$ and $\mathbf{b} = (b_1, \dots, b_N)$ represent the a and b sublattices of the system. The wavenumber k runs over the first BZ, which is $[-\pi, \pi]$. Substituting this ansatz into (14), we obtain the eigenvalue problem $B\mathbf{v} = -\lambda\mathbf{v}$, where $\mathbf{v} = (\mathbf{a}, \mathbf{b})^\top \in \mathbb{C}^{2N}$, B is the $2N \times 2N$ block matrix

$$B = \begin{pmatrix} t_0 + it_2 B_2(k) & t_1 B_1(k) \\ t_1 B_1^\dagger(k) & -t_0 + it_2 B_2^\dagger(-k) \end{pmatrix}, \tag{30}$$

$B_1(k)$ is the $N \times N$ tridiagonal matrix whose rows alternate between $(1, 1, 1)$ and $(1, e^{ik}, 1)$, and $B_2(k)$ is the $N \times N$ pentadiagonal, skew-Hermitian matrix whose rows alternate between $(1, -1 - e^{-ik}, 0, 1 + e^{-ik}, -1)$ and $(1, -1 - e^{ik}, 0, 1 + e^{ik}, -1)$.

When $0 < t_2 < t_2^*$, there is a band gap, but the system does not possess any edge modes (Figure 7, top left). This corresponds to a Chern number of 0 for both bands. As t_2 is increased, the band gap closes at $t_2 = t_2^*$, and then reopens for $t_2 > t_2^*$. A topological transition occurs at $t_2 = t_2^*$, which is concurrent with the band gap closure. For $t_2 > t_2^*$, the Chern numbers of the two bands are ± 1. The resulting topological state is characterized by the appearance of edge modes (blue and red lines in Figure 7, top right) which connect the upper and lower bands. A plot of the associated eigenvectors for these edge modes (Figure 7, bottom) shows that they are indeed localized to the bottom and top edges of the ribbon.

4. Photonic Floquet Topological Insulator

While the Haldane model has not been realized experimentally, it has motivated further theoretical and experimental work in topological photonics. In [RZP+13], Rechtsman et al. performed experiments with a photonic crystal array of coupled, helical waveguides arranged in a honeycomb lattice (as in the Haldane model). The helical waveguides induce temporal modulation of the photonic crystal, which breaks time-reversal symmetry and leads to topological states. We start with the following lattice model, which is a modification of (13) and can be derived from Maxwell's equations (see [AC17, AC22]):

$$\begin{aligned} i\dot{a}_\mathbf{n} + t_1 \sum_{\langle \mathbf{m} \rangle} e^{iR\mathbf{A}(z)\cdot(\mathbf{r_m} - \mathbf{r_n})} b_\mathbf{m} &= 0 \\ i\dot{b}_\mathbf{n} + t_1 \sum_{\langle \mathbf{m} \rangle} e^{iR\mathbf{A}(z)\cdot(\mathbf{r_m} - \mathbf{r_n})} a_\mathbf{m} &= 0, \end{aligned} \tag{31}$$

where the dot denotes differentiation with respect to z, $\mathbf{A}(z) = (\sin(\Omega z), -\cos(\Omega z))^\top$, and the angle brackets indicate that the sum is taken over nearest neighbors. We point out that in the photonics setting, the paraxial direction z is the "time-like" variable. The parameters R and Ω represent the radius of the helical waveguide and its frequency of rotation, respectively. The unit cells $(a_\mathbf{n}, b_\mathbf{n})$ and position vectors $\mathbf{r_n}$ are the same as in the Haldane model, and $\mathbf{r_m} - \mathbf{r_n}$ is the displacement vector between two unit cells. Time-reversal symmetry is broken when $R \neq 0$, since making the transformation $z \mapsto -z$, $(a_\mathbf{n}, b_\mathbf{n}) \mapsto (a_\mathbf{n}^*, b_\mathbf{n}^*)$ and taking complex conjugates takes $R \mapsto -R$ in (31).

We look for solutions of the form

$$\begin{pmatrix} a_\mathbf{n}(z) \\ b_\mathbf{n}(z) \end{pmatrix} = \begin{pmatrix} a(z) \\ b(z) \end{pmatrix} e^{i\mathbf{k}\cdot\mathbf{r_n}}, \tag{32}$$

where the wave vector $\mathbf{k}$ ranges over the first BZ. Unlike the Haldane model, the system (31) is nonautonomous, i.e., it depends on z. As a consequence, the functions $a(z)$ and $b(z)$ will also depend on z. Substituting this ansatz into (31) and simplifying, we obtain the linear, $\mathbf{k}$-dependent, nonautonomous ODE

$$\dot{\mathbf{u}}(z) = iH(z, \mathbf{k})\mathbf{u}(z), \tag{33}$$

where $\mathbf{u} = (a, b)^\top$,

$$\begin{aligned} H(z, \mathbf{k}) &= \begin{pmatrix} 0 & h(z, \mathbf{k}) \\ h^*(z, \mathbf{k}) & 0 \end{pmatrix} \\ h(z, \mathbf{k}) &= t_1 \sum_j e^{-i\mathbf{A}(z)\cdot\delta_j} e^{-i\mathbf{k}\cdot\delta_j}, \end{aligned} \tag{34}$$

and the δ_j are the nearest-neighbor coupling vectors from Figure 4.

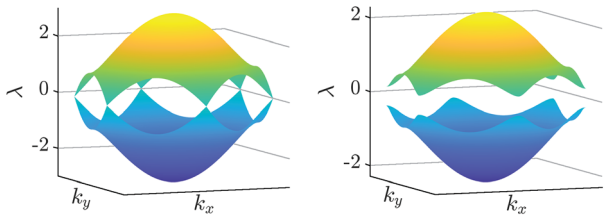

Figure 8. Floquet bands for (33) for $R = 0$ (left) and $R = 1$ (right). Plot shows imaginary part of Floquet exponents over the first BZ. For both cases, $t_1 = 1$, $\Omega = 2\pi$.

Since the matrix $H(z, \mathbf{k})$ is periodic in z with period $T = 2\pi/\Omega$, it follows from Floquet theory (see, for example, [Chi06, Chapter 2.4]) that (33) has solutions of the form $\mathbf{u}(z) = \mathbf{v}(z)e^{\lambda t}$, where $\mathbf{v}(z + T) = \mathbf{v}(z)$, and λ is called a Floquet exponent. To compute the Floquet exponents, let $\Phi(z)$ be the fundamental matrix solution for the system, so that $\mathbf{u}(z) = \Phi(z)\mathbf{u}_0$ is the unique solution to (33) with initial condition $\mathbf{u}_0$. Let $M = \Phi(T)$, which is called the monodromy matrix. The Floquet multipliers μ are the unique eigenvalues of the monodromy matrix M, and the Floquet exponents, which are unique modulo $2\pi i/T$, are related to the Floquet multipliers by $\mu = e^{\lambda T}$. Since the two columns of the monodromy matrix are the unique solutions to (33) at $z = T$ with initial conditions $(1, 0)^\top$ and $(0, 1)^\top$, respectively, it is straightforward to compute the monodromy matrix numerically using a standard ODE solver. Once we have computed M, we can then calculate the Floquet multipliers and exponents numerically.

Figure 8 shows the Floquet band structure of the system, which is obtained by plotting the imaginary part of the Floquet exponents as the wavenumber $\mathbf{k}$ varies over the first BZ (the Floquet exponents are purely imaginary). When $R = 0$, there is no band gap, which is expected since the system reduces to the honeycomb model (13). In this case, the matrix $H(z, \mathbf{k})$ is constant in z, and the Floquet exponents are the eigenvalues of iH. A band gap opens when $R \neq 0$, which can be seen in the right panel of Figure 8. This band gap is associated with a topological state, i.e., a nonzero Chern number. The Chern number for each Floquet band can be computed using the corresponding eigenvector of the monodromy matrix and the numerical method from the previous section. When $R = 0$, the Chern numbers of both bands are 0. For $R \neq 0$ and frequency $\Omega = 2\pi$, the Chern numbers of the two bands are 1 and -1. The edge modes that are a consequence of the nontrivial Chern number are both predicted theoretically and demonstrated experimentally in [RZP+13].

5. Conclusions and Future Directions

In this article, our hope is to illustrate by way of examples the rich mathematics underpinning the study of topological photonics. By confining photons with topological protection, we can generate structures which have applications in topological lasers, buffers, and other optical elements. The signature of these states (e.g., edge modes) is the presence of band gaps in the frequency versus wavenumber dispersion relation. While there have been many experimental demonstrations of these concepts, fully three-dimensional topological photonic bandgaps have not been achieved to date, which is a very promising direction. Another exciting emerging field where mathematical modeling can play an important role is that of quantum topological photonics. In a quantum setting, the application of topological photonics to quantum optics could help to generate robust quantum light sources and protect photons from decoherence during photon propagation.

References

[AC17] Mark J. Ablowitz and Justin T. Cole, *Tight-binding methods for general longitudinally driven photonic lattices: Edge states and solitons*, Phys. Rev. A **96** (2017), Paper No. 043868, DOI 10.1103/PhysRevA.96.043868.

[AC22] Mark J. Ablowitz and Justin T. Cole, *Nonlinear optical waveguide lattices: asymptotic analysis, solitons, and topological insulators*, Phys. D **440** (2022), Paper No. 133440, DOI 10.1016/j.physd.2022.133440. MR4461678

[AOP16] János K. Asbóth, László Oroszlány, and András Pályi, *A short course on topological insulators*: *Band structure and edge states in one and two dimensions*, Lecture Notes in Physics, vol. 919, Springer, Cham, 2016, DOI 10.1007/978-3-319-25607-8. MR3467967

[Ber84] M. V. Berry, *Quantal phase factors accompanying adiabatic changes*, Proc. Roy. Soc. London Ser. A **392** (1984), no. 1802, 45–57, DOI 10.1098/rspa.1984.0023. MR738926

[Chi06] Carmen Chicone, *Ordinary differential equations with applications*, 2nd ed., Texts in Applied Mathematics, vol. 34, Springer-Verlag, New York, 2006, DOI 10.1007/0-387-35794-7.

[FHS05] Takahiro Fukui, Yasuhiro Hatsugai, and Hiroshi Suzuki, *Chern numbers in discretized Brillouin Zone: Efficient method of computing (spin) Hall conductances*, J. Phys. Soc. Jpn. **74** (2005), no. 6, 1674–1677, DOI 10.1143/JPSJ.74.1674.

[Hal88] F. D. M. Haldane, *Model for a quantum Hall effect without Landau levels: Condensed-matter realization of the "parity anomaly"*, Phys. Rev. Lett. **61** (1988), 2015–2018, DOI 10.1103/PhysRevLett.61.2015.

[HR08] F. D. M. Haldane and S. Raghu, *Possible realization of directional optical waveguides in photonic crystals with broken time-reversal symmetry*, Phys. Rev. Lett. **100** (2008), Paper No. 013904, DOI 10.1103/PhysRevLett.100.013904.

[JS14] John D. Joannopoulos and Marin Soljačić, *Topological photonics*, Nature Photonics **8** (2014), 821–829, DOI 10.1038/nphoton.2014.248.

[LCG+22] Zhihao Lan, Menglin L. N. Chen, Fei Gao, Shuang Zhang, and Wei E. I. Sha, *A brief review of topological photonics in one, two, and three dimensions*, Reviews in Physics **9** (2022), Paper No. 100076, DOI 10.1016/j.revip.2022.100076.

[LFR24] J. L. Lado and J. Fernández-Rossier, *Theory of edge states in graphene-like systems*, Encyclopedia of condensed matter physics (second edition), 2024, pp. 350–360, DOI 10.1016/B978-0-323-90800-9.00207-9.
[MS21] Y.-P. Ma and H. Susanto, *Topological edge solitons and their stability in a nonlinear Su-Schrieffer-Heeger model*, Phys. Rev. E **104** (2021), no. 5, Paper No. 054206, DOI 10.1103/physreve.104.054206. MR4349854
[Nak90] Mikio Nakahara, *Geometry, topology and physics*, Graduate Student Series in Physics, Adam Hilger, Ltd., Bristol, 1990, DOI 10.1887/0750306068. MR1065614
[RH08] Srinivas Raghu and Frederick Duncan Michael Haldane, *Analogs of quantum-Hall-effect edge states in photonic crystals*, Phys. Rev. A **78** (2008), no. 3, Paper No. 033834, DOI 10.1103/PhysRevA.78.033834.
[RZP+13] Mikael C. Rechtsman, Julia M. Zeuner, Yonatan Plotnik, Yaakov Lumer, Daniel Podolsky, Felix Dreisow, Stefan Nolte, Mordechai Segev, and Alexander Szameit, *Photonic Floquet topological insulators*, Nature **496** (2013), no. 7444, 196–200, DOI 10.1038/nature12066.
[SSH79] W. P. Su, J. R. Schrieffer, and A. J. Heeger, *Solitons in polyacetylene*, Phys. Rev. Lett. **42** (1979), 1698–1701, DOI 10.1103/PhysRevLett.42.1698.
[Van18] David Vanderbilt, *Berry phases in electronic structure theory: Electric polarization, orbital magnetization and topological insulators*, Cambridge University Press, 2018, DOI 10.1017/9781316662205.
[WCJS08] Zheng Wang, Y. D. Chong, John D. Joannopoulos, and Marin Soljačić, *Reflection-free one-way edge modes in a gyromagnetic photonic crystal*, Phys. Rev. Lett. **100** (2008), Paper No. 013905, DOI 10.1103/PhysRevLett.100.013905.
[WCJS09] Zheng Wang, Yidong Chong, J. D. Joannopoulos, and Marin Soljačić, *Observation of unidirectional backscattering-immune topological electromagnetic states*, Nature **461** (2009), no. 7265, 772–775, DOI 10.1038/nature08293.
[Zak89] J. Zak, *Berry's phase for energy bands in solids*, Phys. Rev. Lett. **62** (1989), 2747–2750, DOI 10.1103/PhysRevLett.62.2747.


Ross Parker


Alejandro Aceves

Credits

Figures 1–8 are courtesy of Ross Parker.
Photo of Ross Parker is courtesy of Sarah Louise Parker.
Photo of Alejandro Aceves is courtesy of Adriana Aceves.